AIP | Journal of Applied Physics

Full-band Monte Carlo simulation of high-energy carrier transport in single photon avalanche diodes with multiplication layers made of InP, InAlAs, and GaAs

Denis Dolgos, Hektor Meier, Andreas Schenk, and Bernd Witzigmann

Citation: J. Appl. Phys. **111**, 104508 (2012); doi: 10.1063/1.4717729
View online: http://dx.doi.org/10.1063/1.4717729
View Table of Contents: http://jap.aip.org/resource/1/JAPIAU/v111/i10
Published by the American Institute of Physics.

Full-band Monte Carlo simulation of high-energy carrier transport in single photon avalanche diodes with multiplication layers made of InP, InAlAs, and GaAs

Denis Dolgos,[1,a)] Hektor Meier,[1] Andreas Schenk,[1] and Bernd Witzigmann[2]
[1]*Integrated Systems Laboratory, ETH Zurich, Gloriastrasse 35, 8092 Zurich, Switzerland*
[2]*Computational Electronics and Photonics Group, University of Kassel, Wilhelmshöher Allee 71, 34121 Kassel, Germany*

(Received 21 March 2012; accepted 12 April 2012; published online 24 May 2012)

We investigate the high-energy charge dynamics of electrons and holes in the multiplication process of single photon avalanche diodes. The technologically important multiplication layer materials InP and $In_{0.52}Al_{0.48}As$, used in near infrared photon detectors, are analyzed and compared with GaAs. We use the full-band Monte Carlo technique to solve the Boltzmann transport equation which improves the state-of-the-art treatment of high-field carrier transport in the multiplication process. As a result of the computationally efficient treatment of the scattering rates and the parallel central processing unit power of modern computer clusters, the full-band Monte Carlo calculation of the breakdown characteristics has become feasible. The breakdown probability features a steeper rise versus the reverse bias for smaller multiplication layer widths for InP, $In_{0.52}Al_{0.48}As$, and GaAs. Both the time to avalanche breakdown and jitter decrease with shrinking size of the multiplication region for the three examined III–V semiconductors. © *2012 American Institute of Physics*. [http://dx.doi.org/10.1063/1.4717729]

I. INTRODUCTION

A. Single photon avalanche diodes

The ability to detect single or few photons enables a variety of innovative applications in the fields of biology, medicine, and physics. For example, the detection of single photons has become an important characteristic for semiconductor circuit diagnostics, security cameras, radiation detection, free space optical communication, or fundamental studies of quantum physics. Fluorescence lifetime imaging is used, for instance, for the research on cell metabolism or the detection of symptoms of diseases. The measurement of the photon arrival time allows the reconstruction of the depth information in three-dimensional laser detection and ranging imaging. One of the most exciting applications for single photon detectors is quantum communication where a single photon carries the information of a bit. Quantum computing and quantum cryptography exploit the quantum mechanical property of entanglement and involve the counting of single photons. The need to transmit single photons over long distances with optical fibers determines the usage of telecommunication wavelengths in the second or third low-absorption window in the near infrared (NIR) spectral range.

Single photon avalanche diodes (SPADs) are reverse biased diodes operated above the breakdown voltage V_b in the Geiger-mode. In principle, a SPAD consists of an absorber region and a multiplication region. The absorber layer is made of a semiconductor material having an appropriate band gap to absorb the desired photon energy by lifting an electron from the valence band into the conduction band. For a sufficiently high band gap, the multiplication layer and the absorption region consist of the same semiconductor because the tunneling rate is acceptable. This is the case for Si SPADs which operate at visible wavelengths.[1] For NIR photon detection, a structure with separated regions of absorption and multiplication is utilized. The absorber is made of a low band gap semiconductor whereas the multiplication layer consists of a semiconductor material with a wider band gap to limit tunneling to an acceptable level. In NIR SPADs, the photon absorber layer is made of $In_{0.53}Ga_{0.47}As$, and the multiplication layer consists of InP[2] or $In_{0.52}Al_{0.48}As$[3] (InAlAs). The utilized material system is lattice-matched. To gain better control over the internal electric field profile, a field control layer separates the absorber and the multiplier (SACM: separate absorption charge and multiplication). Otherwise, a high electric field in the low gap absorption layer leads to tunneling of valence band electrons into the conduction band, and therefore dark counts are initiated. Figure 1 shows the schematic energy band diagram of a NIR SPAD with a SACM structure. A single photon excites an electron-hole pair in the absorption layer. A low electric field separates the pair, and the photogenerated hole drifts into the multiplication layer. The high electric field accelerates the hole to energies where it is able to impact-ionize new electron-hole pairs. The positive feedback loop of impact ionizations launches a self-sustaining charge avalanche. The regulation of the applied bias below the breakdown voltage with an active or passive quenching circuit stops the avalanche. After a hold-off time, the SPAD is biased above the breakdown voltage into its active state.

The first studies on the behavior of avalanche multiplication in reverse biased pn junctions above the breakdown voltage reach back to the Shockley laboratory in the 1960s.[1] Since then, remarkable progress has been achieved for

a)Electronic mail: dolgos@iis.ee.ethz.ch.

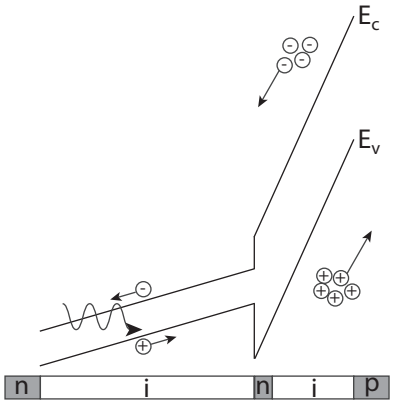

FIG. 1. Schematic energy band diagram of a SACM-structured SPAD with a hole multiplication material like InP. This article concentrates on the charge multiplication process in the gain material.

SPADs concerning their important performance parameters: photon detection efficiency (PDE), dark count rate, jitter, and afterpulsing.[2] The PDE is the product of the quantum efficiency η_q, the probability that the photoexcited carrier survives into the multiplier P_c, and the breakdown probability P_b that the carrier activates a self-sustaining avalanche[2]:

$$\mathrm{PDE} = \eta_q P_c P_b. \tag{1}$$

The PDE depends on the electric field mainly by means of the breakdown probability. The breakdown probability increases with the electric field. Therefore, a higher electric field enhances the photon detection efficiency. On the other hand, band-to-band or trap-assisted tunneling in the multiplication layer initiate dark counts and degrade the performance of SPAD devices for higher electric fields. Hence, to obtain a higher photon detection efficiency for a given increase of the electric field and the tunneling rate, a steep rise of the breakdown probability with the applied bias is favorable. Contradictory predictions of the dependence of the breakdown probability on the multiplicator width have been reported in literature. Wang *et al.*[4] and Ramirez *et al.*[5] predict a rising breakdown probability for thicker multiplication regions using a history-dependent analytical impact ionization model and the recursive dead-space multiplication theory, respectively. On the other hand, Ng *et al.*,[6] Hayat *et al.*,[7] and Tan *et al.*[8] predict the opposite behavior applying the hard dead-space impact ionization model within McIntyre's extended theory, the recurrence equations by McIntyre, and the stochastic random path length model, respectively. The models of Refs. 4–8 rely on simplified impact ionization and charge transport modeling without taking scattering and the dispersion of charge carriers on a microscopic level into account.

The SPAD's timing jitter arises from various sources. The location of the photon absorption varies; it causes different transit times of the particles into the multiplication layer. Trapped carriers at possible heterojunctions are randomly released. The avalanche build-up time t_b fluctuates due to the randomness of the impact ionization process, the expansion of the initially point-like avalanche to the entire high-field region, and local nonuniformities of the excess bias. The avalanche build-up time is the main contribution to the timing jitter[2]

$$\sigma = \sqrt{\langle t_b^2 \rangle - \langle t_b \rangle^2}. \tag{2}$$

B. High-energy charge dynamics

At present, the full-band Monte Carlo (FBMC) solution of the Boltzmann transport equation is the most accurate device simulation method for semiclassical charge transport.[9,10] The FBMC approach serves as the benchmark for approximate methods. Application of the FBMC technique with the most comprehensive band structure description and appropriate scattering models improves the state-of-the-art treatment of high-energy charge transport in the multiplication process of single photon avalanche diodes. On the deca-nanometer length scale, nonequilibrium effects like the velocity overshoot, dead-space, and nonlocal impact ionization become important. They are naturally covered by the Monte Carlo technique. The FBMC simulations involve a high computational burden. However, combining the parallel central processing unit (CPU) power of modern standard computer clusters with computationally efficient approaches,[9] FBMC simulations have become feasible. The gain of sufficient data to render statistics has become practicable for the evaluation of breakdown probabilities and the standard deviations of variables of interest. This article's focus is on the high-energy charge transport in the multiplication process of SPADs with multiplicator layers made of InP, InAlAs, and GaAs. The effect of tunneling is not considered.

II. FULL-BAND MONTE CARLO MODEL

Concerning the details of our full-band Monte Carlo simulator *CarloS* and the approximations of the scattering model, we refer to Ref. 11 and the references therein. This paragraph gives a brief overview of the underlying transport model. We use a three-dimensional equidistant tensor grid to mesh the irreducible wedge of the first Brillouin zone and a one-dimensional tensor grid for the real-space discretization. The length of a cubic box is $l = 0.01 \times 2\pi/a$ with the lattice constant a. This leads to a total number of 87 125 cubes discretizing the irreducible wedge. The one-dimensional tensor grid for the real-space discretization has a spacing of 1 nm. We compute the full-band structures by means of the empirical pseudopotential method using parameters from Ref. 12. Figure 2 shows the dispersion relations along special paths through the Brillouin zone. The charged particles propagate according to Newton's law[13] with a simple time-step propagation scheme.[14] A drift-diffusion model[15] is used to precompute the electric field profile. The full-band computation of the breakdown characteristics of SPADs causes a huge computational effort. Approximations of the scattering rates have to be made that render the FBMC computation feasible while the main physical features have to be kept. The main contribution to the variation of carrier-phonon scattering rates with the particle energy is a result of the available density of final states. The transition matrix elements are

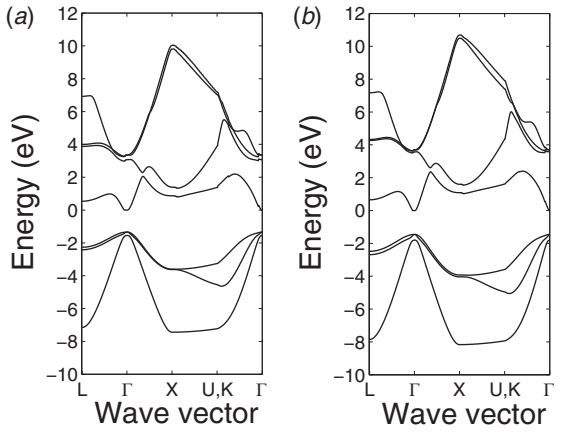

FIG. 2. Band structure of (a) InP and (b) InAlAs. Concerning the band structure of GaAs, we refer to Ref. 11.

approximately constant within the valleys of the reciprocal space.[16–20] Therefore, a computationally very efficient formulation of the carrier-phonon scattering rates is possible.[9] We utilize the method by Gilat and Raubenheimer[21] to integrate δ-functions which emerge in Fermi's golden rule. Figure 3 presents the total carrier-phonon and the impact ionization scattering rates.

TABLE I. Scattering rate prefactors Λ for the different scattering mechanisms. The quantities are the Boltzmann constant k_B, lattice temperature T, acoustic phonon deformation potential Ξ_ν, reduced Planck constant $\hbar$, longitudinal sound velocity u_l, mass density of the semiconductor material ρ, optical and intervalley phonon deformation potential D_ν and $D_{\nu\nu'}$, optical and intervalley phonon occupation number n_{op} and $n_{\nu\nu'}$, optical and intervalley phonon angular frequency ω_{op} and $\omega_{\nu\nu'}$, elementary charge e, polar coupling constant in Fröhlich expression F, impact ionization matrix element M_{ii}, crystal volume V, and number of unit cells N.

Scattering mechanism	Λ
Elastic acoustic phonon scattering	$\frac{\pi k_B T \Xi_\nu^2}{\hbar u_l^2 \rho}$
Nonpolar optical phonon scattering	$\frac{\pi D_\nu^2}{2\rho\omega_{\text{op}}}\left(n_{\text{op}} + \frac{1}{2} \mp \frac{1}{2}\right)$
Intervalley phonon scattering	$\frac{\pi D_{\nu\nu'}^2}{2\rho\omega_{\nu\nu'}}\left(n_{\nu\nu'} + \frac{1}{2} \mp \frac{1}{2}\right)$
Polar optical phonon scattering	$\frac{2\pi}{\hbar} e^2 F^2 \left(n_{\text{op}} + \frac{1}{2} \mp \frac{1}{2}\right)$
Impact ionization	$\frac{2\pi}{\hbar} \lvert M_{\text{ii}} \rvert^2 \frac{V^3}{N}$

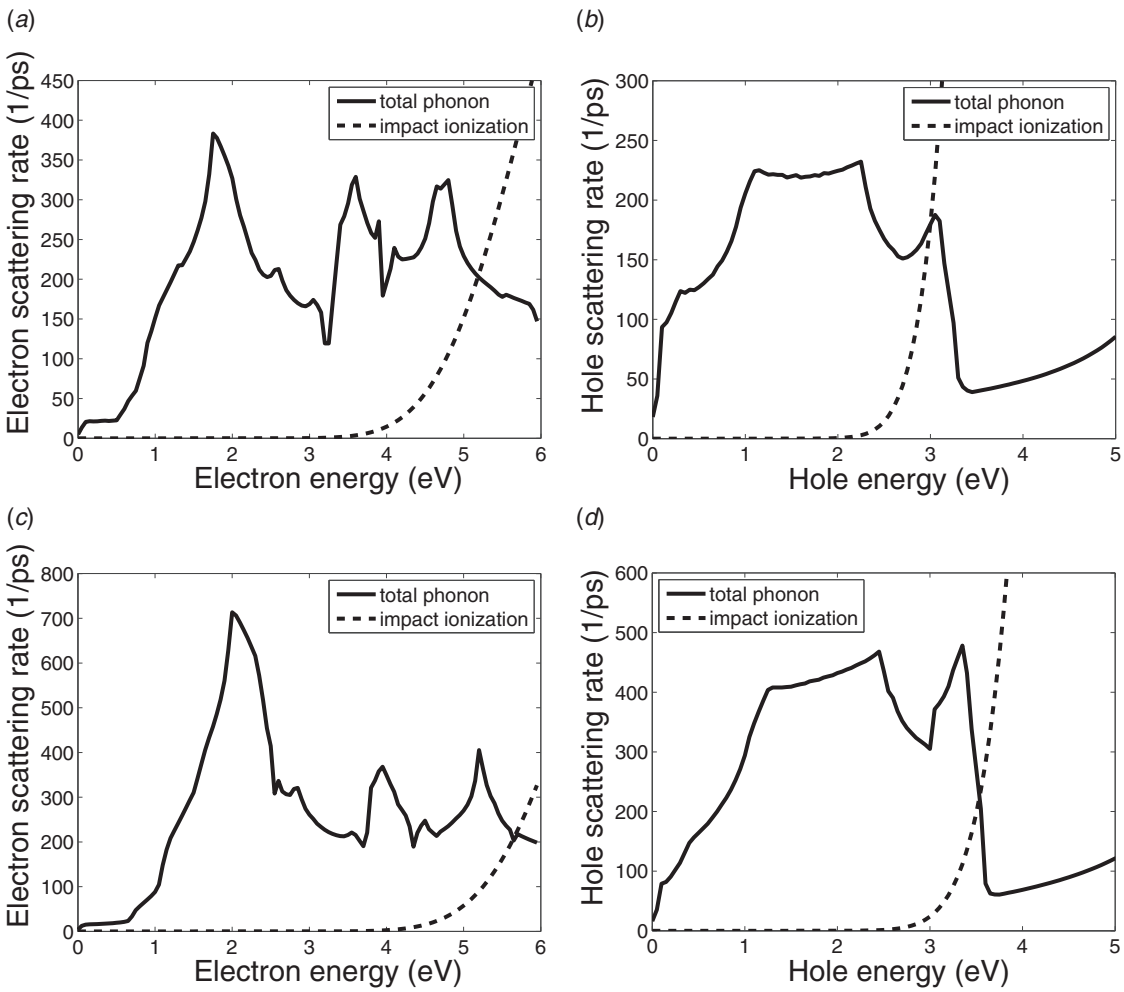

FIG. 3. Full-band carrier-phonon and impact ionization scattering rates of (a, b) InP and (c, d) InAlAs. The full-band scattering rates of GaAs have been published in Ref. 11.

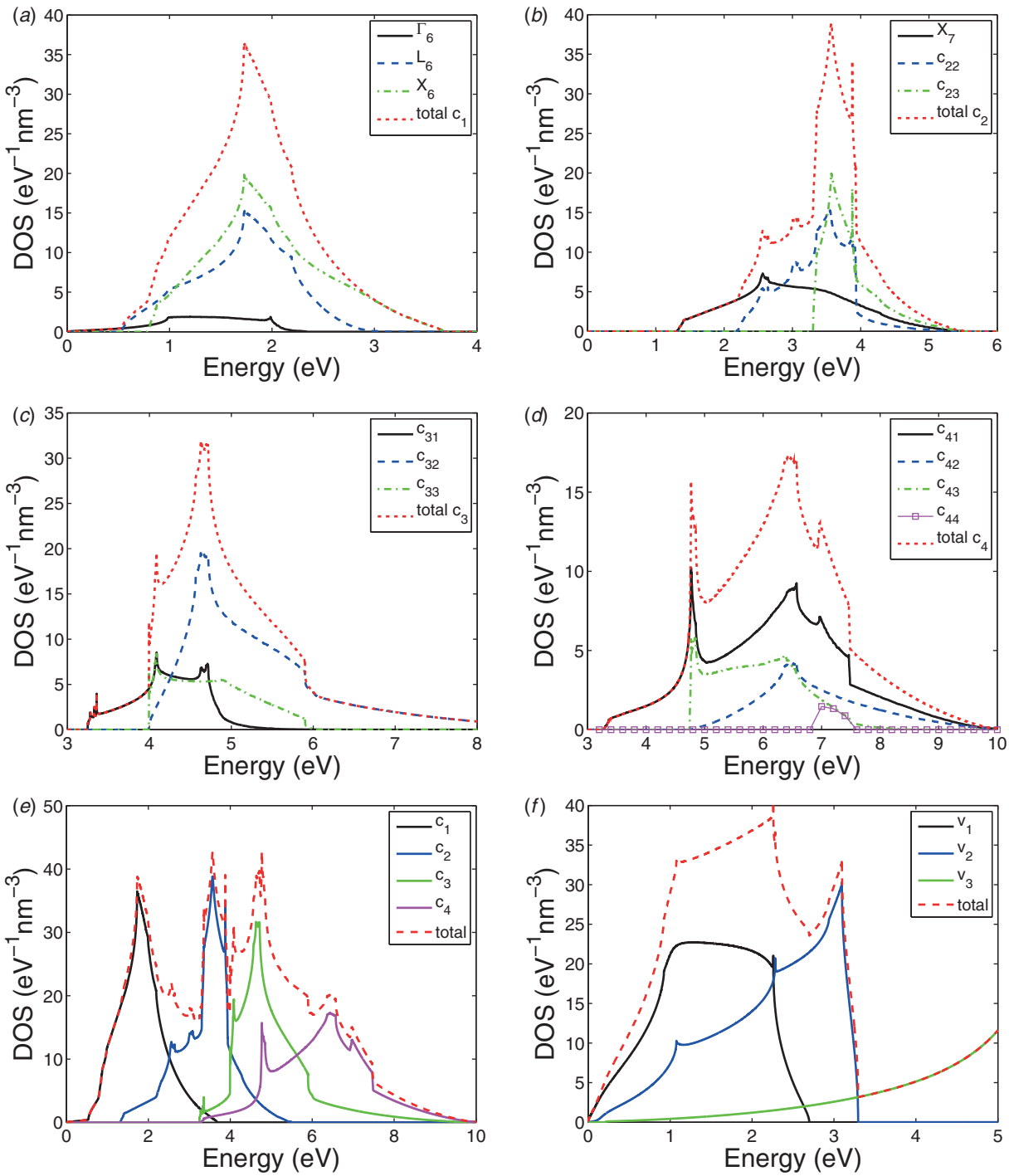

FIG. 4. Valley DOS of InP for (a–d) conduction bands 1–4 and the total contribution of the (e) conduction bands and the (f) valence bands.

Three forms of scattering mechanisms appear that differ in their proportionality functions: (i) elastic acoustic phonon scattering, nonpolar optical phonon scattering, intervalley phonon scattering, alloy scattering; (ii) polar optical phonon scattering; and (iii) impact ionization scattering. Table I summarizes the coupling strenghts for the different scattering mechanisms.

Scattering rates of the first form are given by

$$W^m_{\nu\nu'}(E) = \Lambda^m_{\nu\nu'}\mathcal{D}_{\nu'}(E \pm E_{\text{trans}}) \tag{3}$$

with the particle energy E before and $E' = E \pm E_{\text{trans}}$ after scattering, the transition energy E_{trans} of the carrier-phonon interaction process, the prefactor $\Lambda^m_{\nu\nu'}$ of the scattering mechanism type m, and the initial valley ν and the final valley ν'. The scattering rate is proportional to the final DOS (Ref. 22) including spin degeneracy

$$\mathcal{D}_{\nu'}(E) = \frac{1}{4\pi^3}\int_{V_{\nu'}} \delta(E - E_{\nu'}(\mathbf{k}'))d^3k' = \frac{1}{4\pi^3}\int_{E_{\nu'}(\mathbf{k})=E(\mathbf{k})} \frac{dA}{|\nabla_{\mathbf{k}}E_{\nu'}(\mathbf{k})|}. \tag{4}$$

Figures 4 and 5 present the numerically evaluated full-band valley DOS for InP and InAlAs. The valley DOS of GaAs

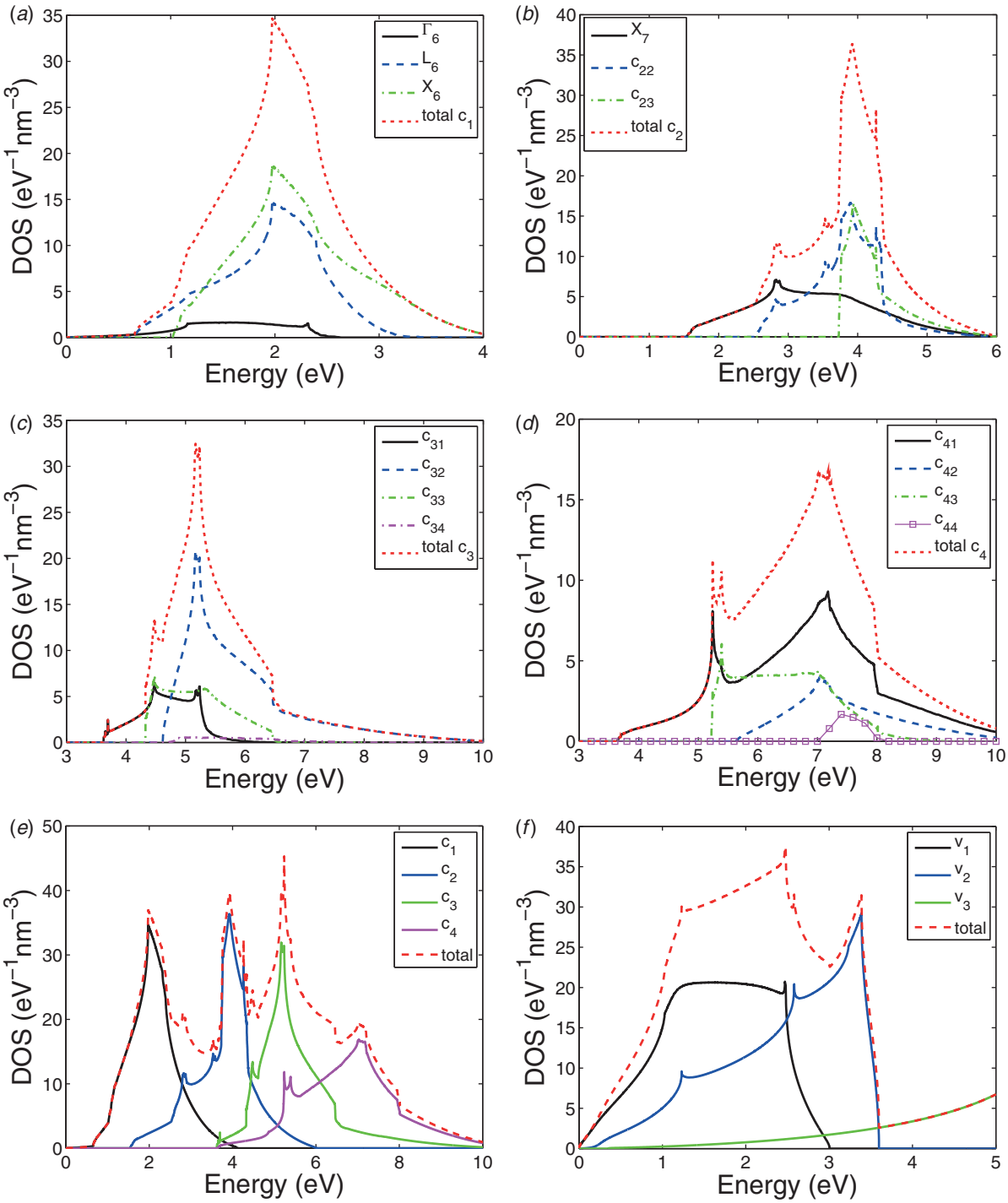

FIG. 5. Valley DOS of InAlAs for (a–d) conduction bands 1–4 and the total contribution of the (e) conduction bands and the (f) valence bands.

has been published in Ref. 11. The first four conduction band valleys are Γ_6, L_6, and X_6 for the first conduction band, and X_7 for the second conduction band. All other conduction band valleys are defined as c_{nm} with the conduction band number n and the valley number m within n. The valleys are ordered with rising valley minimum energy within a band.

The polar optical phonon scattering rate is of the second form

$$W_{\nu'}^{\text{pop}}(E) = \Lambda^{\text{pop}} \mathcal{D}_{q^{-2},\nu'}(E) \tag{5}$$

with its prefactor Λ^{pop}. The rate is proportional to the direction-weighted DOS including spin degeneracy

$$\mathcal{D}_{q^{-2},\nu'}(\mathbf{k}) = \frac{1}{4\pi^3}\int \frac{1}{|\mathbf{q}|^2}\delta(E_{\nu'}(\mathbf{k}') - E(\mathbf{k}) \mp \hbar\omega_{\text{op}})d^3k'$$
$$= \frac{1}{4\pi^3}\int_{E_{\nu'}(\mathbf{k}')=E(\mathbf{k})\pm\hbar\omega_{\text{op}}} \frac{dA(E(\mathbf{k}) \pm \hbar\omega_{\text{op}})}{|\mathbf{q}|^2|\nabla_{\mathbf{k}'}(E(\mathbf{k}) \pm \hbar\omega_{\text{op}})|} \tag{6}$$

with the phonon wave vector $\mathbf{q} = \mathbf{k} - \mathbf{k}'$. The anisotropic polar optical phonon scattering rate is averaged according to[23]

$$W(E) = \frac{1}{\mathcal{D}(E)}\sum_{\mathbf{k}} W(\mathbf{k})\delta(E(\mathbf{k}) - E) \tag{7}$$

TABLE II. Fit parameters for InP, InAlAs, and GaAs. The three values of the acoustic phonon deformation potential of electrons in InAlAs correspond to the Γ_6-, L_6-, and X_6-valley, respectively (compare with Mateos *et al.*[26]).

Particle	Material	$\Xi_<$ (eV)	Ξ (eV)	$D_<\left(\frac{\text{eV}}{\text{nm}}\right)$	$D\left(\frac{\text{eV}}{\text{nm}}\right)$	Λ^{alloy} (eV)	$\Lambda^{\text{ii}}\left(\frac{\text{nm}^9\text{eV}}{\text{ps}}\right)$	$E_{\text{th}}^{\Gamma_6}$ (eV)
Electrons	InP	7.0	5.0	0.0	20	…	0.012	0.4
	InAlAs	…	5.9/7.2/9.0	…	30	0.47	2×10^{-2}	0.0
	GaAs	7.0	5.0	0.0	19	…	0.03	0.4
Holes	InP	…	5.0	…	25	…	1.0	0.0
	InAlAs	…	4.3	…	43	0.38	1.0	0.0
	GaAs	…	5.0	…	50	…	1.0	0.0

with the initial density of states $\mathcal{D}(E)$.

The impact ionization scattering rate defines the third form

$$W^{\text{ii}}(E) = \Lambda^{\text{ii}}\mathcal{D}_{\text{ii}}(E) \tag{8}$$

with its prefactor Λ^{ii}. The impact ionization scattering rate is proportional to the density of states overlap integral $\mathcal{D}_{\text{ii}}$. For impacting electrons, it is given by

$$D_{\text{ii}}(E_c) = \sum_{\substack{v'c'c'' \\ c''\geq c'}} \int_0^{\hat{E}_{c'}} dE_{c'} \int_0^{\hat{E}_{v'}} dE_{v'} D_{v'}(E_{v'}) D_{c'}(E_{c'}) \times D_{c''}(E_c - E_{c'} - E_{v'} - E_g). \tag{9}$$

The integration boundaries are $\hat{E}_{c'} = E_c - E_g$ and $\hat{E}_{v'} = E_c - E_{c'} - E_g$. Furthermore, E_g is the band gap energy. Swapping the indices for the conduction band c and valence band v leads to the expression for a primary impacting hole.

III. CALIBRATION OF COUPLING STRENGTHS

As a result of the empirical deformation potential ansatz and the impact ionization ansatz, the carrier-phonon coupling strengths have to be calibrated to fit to experimental data.[18,23] Fitting the FBMC curves of the drift velocity versus the electric field against experimental data determines

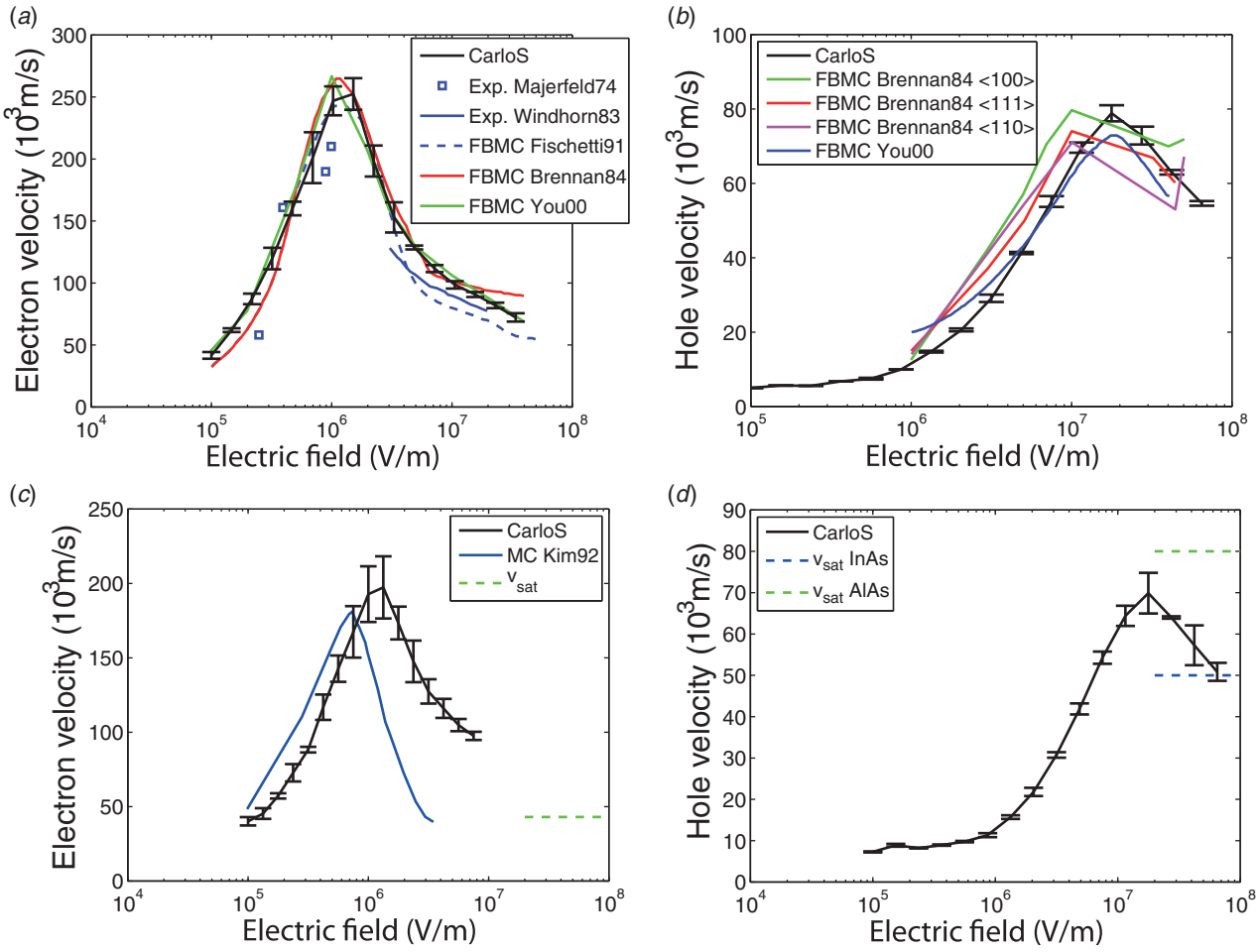

FIG. 6. Calibration results for the velocity vs. electric field for electrons and holes in (a, b) InP and (c, d) InAlAs. The calibration results of GaAs have been published in Ref. 11.

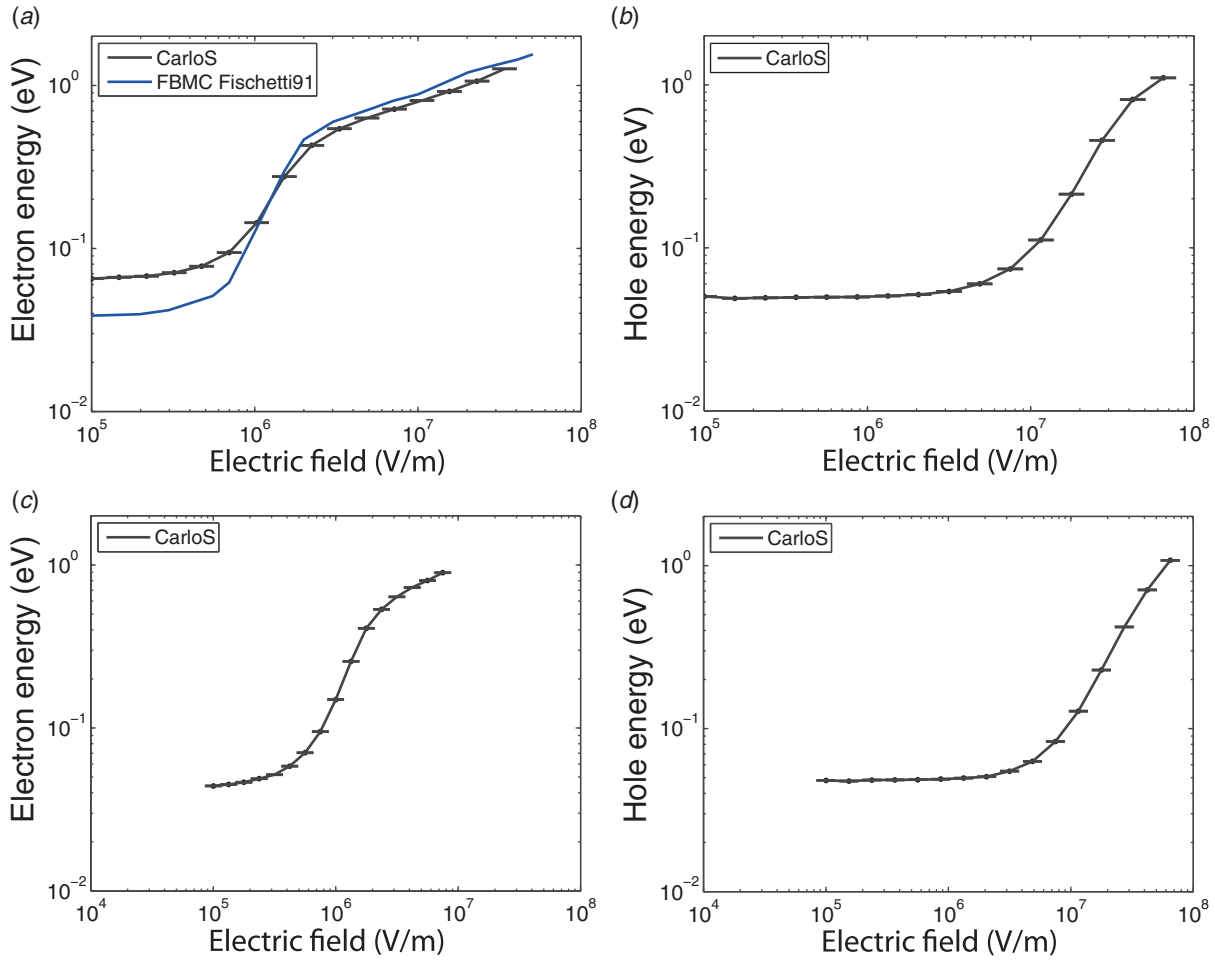

FIG. 7. Calibration results for the energy vs. electric field for electrons and holes in (a, b) InP and (c, d) InAlAs.

the carrier-phonon coupling strengths. Calibrating the FBMC impact ionization coefficients α and β for electrons and holes versus the inverse electric field against experimental data designates the impact ionization parameters. Differences in the calibration results among the FBMC modeling groups have to be expected because the dependency of some fitting parameters on the experimental data is weak.[24] In addition, the underlying dispersion relations of the FBMC simulators used in literature vary especially for higher carrier energies.

Table II outlines the calibrated parameters for InP, InAlAs, and GaAs. The acoustic phonon deformation potential for electrons reads

$$\Xi_\nu = \begin{cases} \Xi_< & \text{if } E < E_{\text{th}}^{\Gamma_6} \text{ and } \nu = \Gamma_6, \\ \Xi & \text{else,} \end{cases} \tag{10}$$

and the nonpolar optical phonon deformation potential for electrons is given by

$$D_\nu = \begin{cases} D_< & \text{if } E < E_{\text{th}}^{\Gamma_6} \text{ and } \nu = \Gamma_6, \\ D & \text{else.} \end{cases} \tag{11}$$

Here, $\Xi_<$ and $D_<$ label the electron-phonon deformation potentials for electron energies below the energy threshold $E_{\text{th}}^{\Gamma_6}$ for the analytical treatment in the Γ_6-valley (compare with Fischetti and Laux[23]). Concerning the details of the nonparabolic treatment of the band structure for low-energy electrons in the Γ_6-valley, the authors refer to Jacoboni and Reggiani.[25] The holes in InP, InAlAs, and GaAs simply possess one value of the deformation potential in each case for the heavy hole, light hole, and split-off band.

Figures 6, 7, and 8 summarize the calibration results and compare them with experiments and other FBMC simulations from literature: Armiento83,[27] Brennan84,[28] Cook82,[29] Dunn97,[30] Fischetti91,[24] Kim92,[31] Majerfeld74,[32] Taguchi86,[33] Watanabe90,[34] Windhorn83,[35] and You00.[36] The electron and hole saturation velocities v_{sat} of InAlAs are taken from Zhou *et al.*[37] and Palankovski and Quay.[38] The bars of length 2σ indicate the 68% confidence interval.

IV. SIMULATION RESULTS AND DISCUSSION

In this article, we concentrate on the simulation of the high-energy charge transport of the multiplication process in the SPAD's multiplication layer. Therefore, according to Tan *et al.*,[8] PIN diode structures are investigated with different intrinsic region widths w between 55 nm and 500 nm operated in the Geiger-mode. In order to compare the SPAD simulations with literature, the temperature is set to $T = 300$ K. We investigate the multiplication layer materials InP and InAlAs which are utilized in real-world SPAD devices and

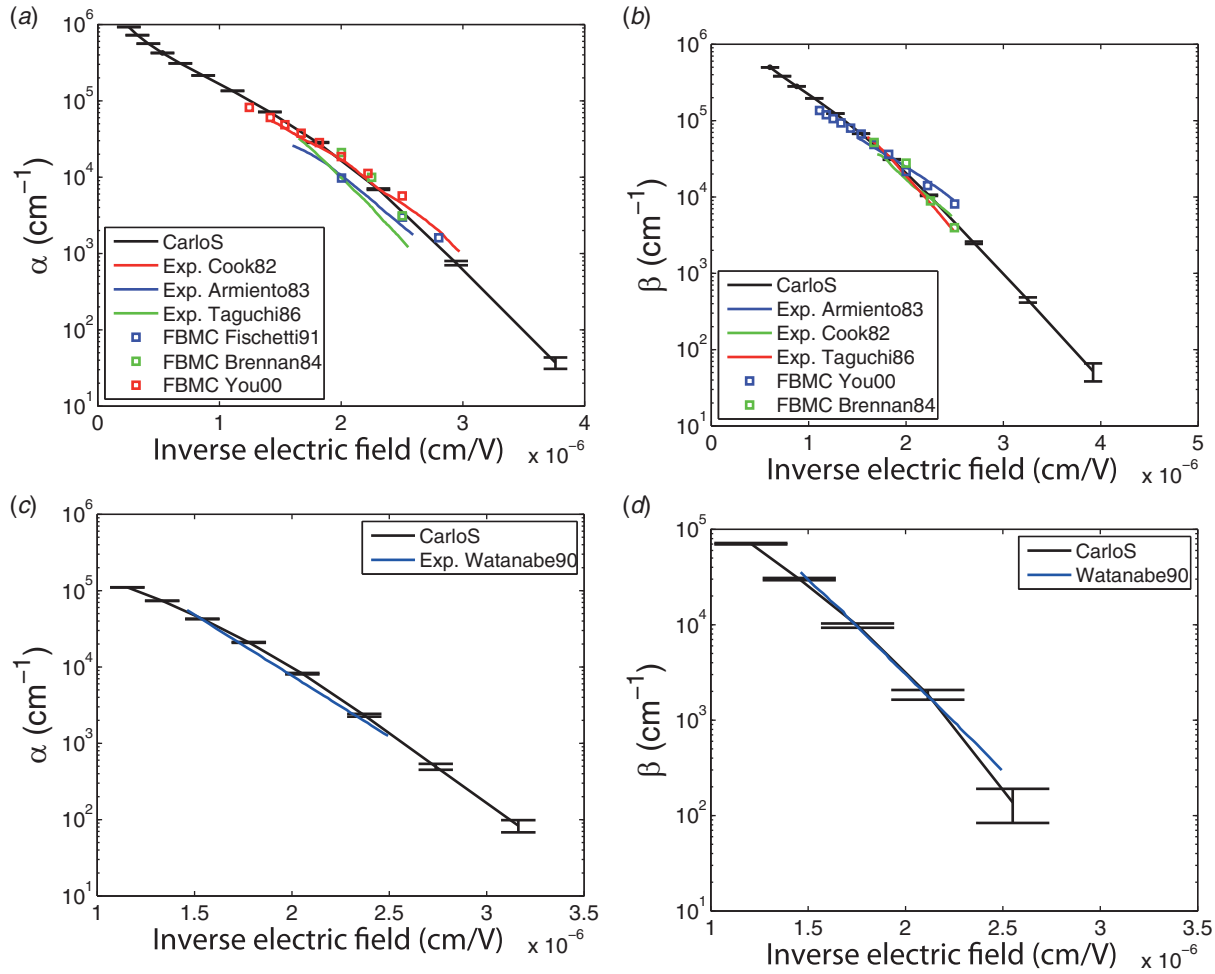

FIG. 8. Calibration results for the impact ionization coefficients vs. inverse electric field for electrons and holes in (a, b) InP and (c, d) InAlAs. The calibration results of GaAs have been published in Ref. 11.

compare them with GaAs. This work examines the breakdown probability, which is the main contribution to the PDE, and the time to avalanche breakdown. In addition, the standard deviation of the time to avalanche breakdown is calculated which is the main contribution to the timing jitter. The simulation procedure consists of a single electron injection for InAlAs and GaAs and a single hole injection for InP with an energy of 10 meV at the time $t = 0$ ps into the PIN diode. Compared to Ref. 11, we chose a slightly different boundary condition of the carrier's injection position. In this work, the injected carriers start their propagation in a region of higher electric field strengths farther inside the simulation domain. The injected carriers that start in a region of lower electric field leave the simulation domain more frequently due to backscattering than carriers injected into a region of higher electric fields. Therefore, the breakdown probability saturates more quickly toward unity. By definition, breakdown occurs when the total number of charge carriers within the simulation domain, generated by impact ionization, exceeds 30. The simulation stops in the case when a breakdown has not taken place within 500 ps. To gain sufficient statistics, we have rerun the numerical experiments 2500 times per reverse bias point. A breakdown criterion that leads to an early stop of the FBMC simulation of the avalanche build-up makes the computation of SPAD statistics feasible on standard computer clusters. Small currents, estimated with Ramo's theorem,[39] and hence few carriers in the simulation domain, possess high fluctuations. A breakdown criterion with higher currents is computationally too expensive to render FBMC simulations.

Figure 9 presents the breakdown probability versus the reverse bias V_r and excess bias $V_{ex} = V_r - V_b$ for the different gain materials and multiplication layer widths. The definition of the breakdown voltage V_b is $P_b(V_b) = 10^{-3}$. Three regions characterize the dependency of the breakdown probability on reverse bias (compare with Ref. 11). For InP, InAlAs, and GaAs, P_b increases slightly after the breakdown voltage. For higher V_r, the breakdown probability depends linearly on the reverse bias. Then, P_b saturates toward unity. Tosi *et al.*[40] and Campbell and Hu[41] experimentally confirm the linear rise after the breakdown voltage for an InGaAs/InP SPAD. The smaller the multiplication region, the steeper the rise of P_b with a higher reverse bias for all three examined gain materials. GaAs exhibits the steepest slope. GaAs is followed by InP and InAlAs for the devices having $w = 55$ nm and $w = 250$ nm. For the SPAD with the multiplication region width of $w = 500$ nm, GaAs is followed by InAlAs and InP. A steep rise of P_b versus V_r is advantageous because the photon detection efficiency is higher for the same applied excess bias. However, the electric field rises

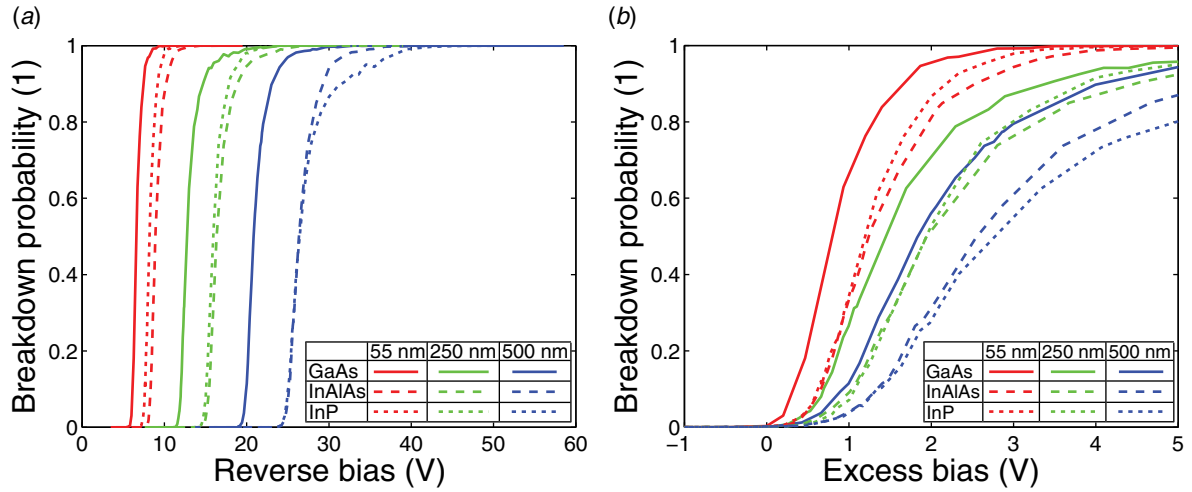

FIG. 9. Comparison of the breakdown probability vs. (a) reverse bias and (b) excess bias for SPADs consisting of the multiplication layer materials InP, InAlAs, and GaAs.

in thinner structures leading to an increased tunneling probability and dark counts. The region of saturation is larger for increasing multiplicator widths. Compared to the simpler models of Refs. 4–8, the FBMC simulations predict a less steep rise of the breakdown probability with the reverse bias.

The decrease of the multiplication layer width, while keeping the applied bias constant, results in two factors that affect the charge avalanche positively and negatively. On the one hand, the smaller w, the higher the electric field strength in the multiplication region. This fact leads to two consequences that enforce the avalanche. First, a higher electric field entails higher values of the impact ionization coefficients α and β. Thus, impact ionization takes place more often. Second, the ratio of the impact ionization coefficients k tends to unity (compare with Fig. 8) for higher electric fields. The ratio $k \approx 1$ leads to a more prominent positive feedback of the impact ionization process.[42] On the other hand, two negative implications for the charge avalanche result for shrinking multiplication layer widths. First, the smaller w, the shorter the available gain material length. Second, the relative contribution of the dead-space d to the multiplicator width rises for smaller w. Therefore, a higher d/w ratio corresponds to a further reduction of the effective multiplication region thickness. Finally, the balance between the positive feedback of the charge avalanche and the reduction of the effective length of the gain material governs the behavior of the breakdown probability steepness for changing multiplication widths.[6,8,11] The numerical computation of the high-energy charge dynamics of the charge multiplication process with the FBMC technique reveals the dominance of the positive feedback over the reduction of the effective gain material width for the three investigated materials.

Figure 10 illustrates the mean time to avalanche breakdown $\langle t_b \rangle$ and its jitter σ versus the excess bias. For an increasing excess bias, the mean time to avalanche breakdown and its jitter decrease exponentially. This finding agrees with experimental data available for InGaAs/InP SPADs.[3] Two regions characterize the dependency of the mean time to avalanche breakdown and its jitter on excess bias. For InP, InAlAs, and GaAs, $\langle t_b \rangle$ and σ decline steeply after P_b. Then, for higher excess biases the quantities feature a less steep decrease. The shorter the multiplication layer

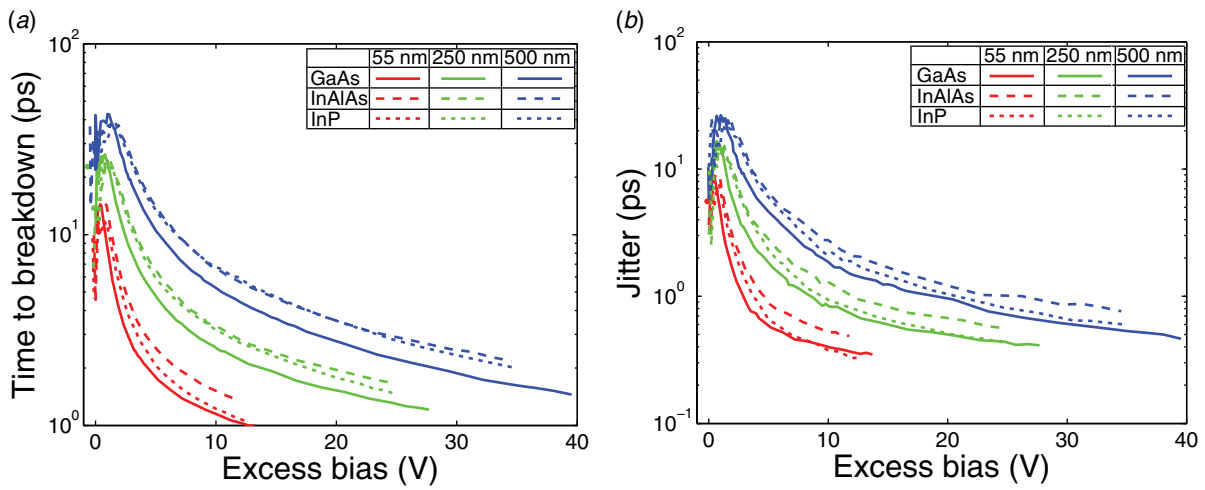

FIG. 10. Comparison of (a) the time to avalanche breakdown and (b) its jitter vs. excess bias for SPADs consisting of the multiplication layer materials InP, InAlAs, and GaAs.

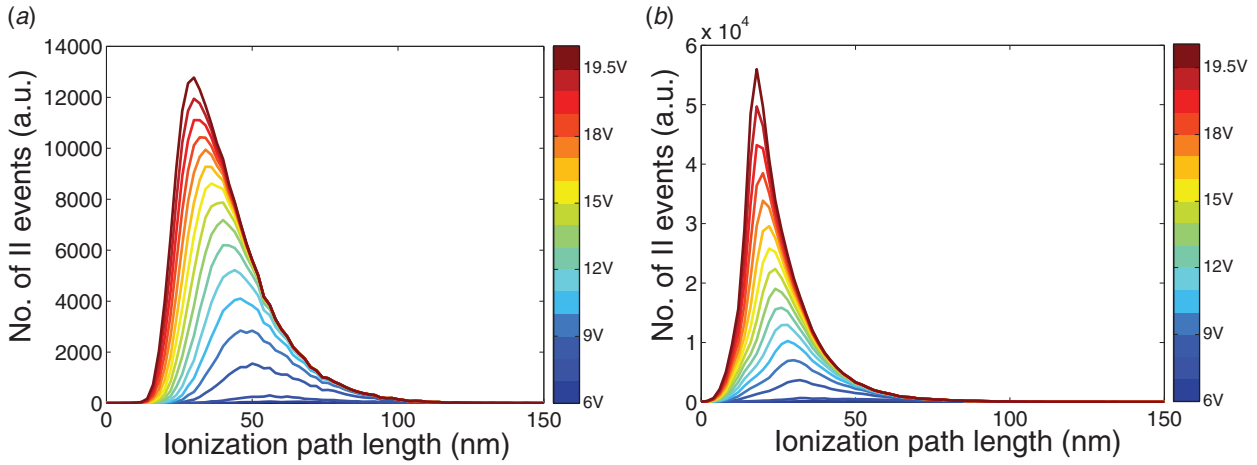

FIG. 11. Distribution of the number of impact ionization (II) events vs. the ionization path length for (a) electrons and (b) holes. The SPAD consists of the multiplication layer material InP and has a width of 55 nm. The color map indicates the applied reverse voltage.

width, the smaller the time till the avalanche breakdown and the smaller its jitter. Additionally, $\langle t_b \rangle$ and σ descend sharper for smaller w. Concerning the time to breakdown and its jitter, GaAs exhibits the best characteristics followed by InP and InAlAs. For example, increasing the excess bias from 0.5 V to 5 V at the GaAs SPAD with $w = 55$ nm leads to a reduction of $\langle t_b \rangle$ and σ of about one order of magnitude.

Figure 11 depicts the number of impact ionization events versus the ionization path length of electrons and holes in the SPAD made of InP with $w = 55$ nm. The normalized curves result in the probability density functions of the ionization path lengths. For increasing electric fields, the total number of the impact ionization events rises and the distribution narrows. The mean values of the impact ionization path length and the dead-spaces become shorter for higher applied voltages.

V. CONCLUSION

In summary, we have simulated the charge multiplication process in InP, InAlAs, and GaAs SPADs by means of the currently most accurate device simulation method for high-energy carrier transport. This improves the state-of-the-art treatment of high-field carrier dynamics in single photon avalanche diodes. Attention has been paid to achieve computationally efficient scattering expressions. All scattering rates in a given material have been calculated based on the same band structure, thus keeping band structure consistency. As a result of the computationally efficient treatment of the scattering rates and the parallel CPU power of modern computer clusters, the FBMC simulation of SPAD breakdown characteristics has become feasible. Highly nonequilibrium effects like the dead-space, nonlocal impact ionization, and velocity overshoot are incorporated with the full-band Monte Carlo technique. We have analyzed the behavior of the breakdown probability, time to avalanche breakdown, and its jitter for different multiplication region widths ranging from 55 nm to 500 nm. For the examined gain materials InP, InAlAs, and GaAs, the breakdown probability exhibits a steeper rise with the reverse bias for decreasing multiplicator sizes. Additionally, the mean time to avalanche breakdown and its jitter diminish for shorter multiplication widths. Concerning the photon detection efficiency, photon detection speed, and noise owing to the stochastic avalanche build-up, full-band Monte Carlo simulations suggest the usage of smaller multiplication region widths for a given excess bias. Our FBMC simulations exhibit that the positive avalanche feedback dominates over the reduction of the effective gain material width for decreasing multiplicator layer sizes. GaAs exhibits the best breakdown characteristics followed by InP and InAlAs.

[1]S. Cova, M. Ghioni, A. Lotito, I. Rech, and F. Zappa, "Evolution and prospects for single-photon avalanche diodes and quenching circuits," J. Mod. Opt. **51**, 1267–1288 (2004).
[2]M. Itzler, X. Jiang, M. Entwistle, K. Slomkowski, A. Tosi, F. Acerbi, F. Zappa, and S. Cova, "Advances in InGaAsP-based avalanche diode single photon detectors," J. Mod. Opt. **58**, 174–200 (2011).
[3]M. A. Itzler, R. Ben-Michael, C. F. Hsu, K. Slomkowski, A. Tosi, S. Cova, F. Zappa, and R. Ispasoiu, "Single photon avalanche diodes (SPADs) for 1.5 μm photon counting applications," J. Mod. Opt. **54**, 283–304 (2007).
[4]S. Wang, F. Ma, X. Li, G. Karve, X. Zheng, and J. C. Campbell, "Analysis of breakdown probabilities in avalanche photodiodes using a history-dependent analytical model," Appl. Phys. Lett. **82**, 1971 (2003).
[5]D. Ramirez, M. Hayat, G. Karve, J. Campbell, S. Torres, B. Saleh, and M. Teich, "Detection efficiencies and generalized breakdown probabilities for nanosecond-gated near infrared single-photon avalanche photodiodes," IEEE J. Quantum Electron. **42**, 137–145 (2006).
[6]J. Ng, C. Tan, J. David, and G. Rees, "Theoretical study of breakdown probabilities in single photon avalanche diodes," in *IEEE Lasers and Electro-Optics Society (LEOS) Annual Meeting (*IEEE, 2003), pp. 773–774.
[7]M. Hayat, U. Sakoglu, J. Campbell, B. Saleh, and M. Teich, "Breakdown probabilities for thin heterostructure avalanche photodiodes," IEEE J. Quantum Electron. **39**, 179–185 (2003).
[8]S. L. Tan, D. S. Ong, and H. K. Yow, "Theoretical analysis of breakdown probabilities and jitter in single-photon avalanche diodes," J. Appl. Phys. **102**, 044506 (2007).
[9]C. Jungemann, S. Keith, M. Bartels, and B. Meinerzhagen, "Efficient full-band Monte Carlo simulation of silicon devices," IEICE Trans. Electron. **E82C**, 870–879 (1999).
[10]K. Hess, *Monte Carlo Device Simulation: Full Band and Beyond* (Kluwer Academic, Dordrecht, 1991).
[11]D. Dolgos, H. Meier, A. Schenk, and B. Witzigmann, "Full-band Monte Carlo simulation of high-energy carrier transport in single photon avalanche diodes: computation of breakdown probability, time to avalanche breakdown, and jitter," J. Appl. Phys. **110**, 084507 (2011).
[12]J. R. Chelikowsky and M. L. Cohen, "Nonlocal pseudopotential calculations for the electronic structure of eleven diamond and zinc-blende semiconductors," Phys. Rev. B **14**, 556–582 (1976).

[13]F. M. Bufler, *Full-Band Monte Carlo Simulation of Nanoscale Strained-Silicon MOSFETs* (Hartung-Gorre, Konstanz, 2003).
[14]F. M. Bufler, A. Schenk, and W. Fichtner, "Proof of a simple time-step propagation scheme for Monte Carlo simulation," Math. Comput. Simul. **62**, 323–326 (2003).
[15]Synopsys, Inc., *Sentaurus Device User Guide, Version Y-2006.06* (Synopsys, Inc., Mountain View, CA, USA, 2006).
[16]A. Abramo, L. Baudry, R. Brunetti, R. Castagne, M. Charef, F. Dessenne, P. Dollfus, R. Dutton, W. Engl, R. Fauquembergue, C. Fiegna, M. Fischetti, S. Galdin, N. Goldsman, M. Hackel, C. Hamaguchi, K. Hess, K. Hennacy, P. Hesto, J. Higman, T. Iizuka, C. Jungemann, Y. Kamakura, H. Kosina, T. Kunikiyo, S. Laux, C. Maziar, H. Mizuno, H. Peifer, S. Ramaswamy, N. Sano, P. Scrobohaci, S. Selberherr, M. Takenaka, K. Taniguchi, J. Thobel, R. Thoma, K. Tomizawa, M. Tomizawa, T. Vogelsang, P. Yoder, and A. Yoshii, "A comparison of numerical solutions of the Boltzmann transport equation for high-energy electron transport silicon," IEEE Trans. Electron Devices **41**, 1646–1654 (1994).
[17]T. Kunikiyo, M. Takenaka, Y. Kamakura, M. Yamaji, H. Mizuno, M. Morifuji, K. Taniguchi, and C. Hamaguchi, "A Monte Carlo simulation of anisotropic electron transport in silicon including full band structure and anisotropic impact-ionization model," J. Appl. Phys. **75**, 297–312 (1994).
[18]M. V. Fischetti and S. E. Laux, "Monte Carlo simulation of electron transport in Si: the first 20 years," in *ESSDERC'96. Proceedings of the 26th European Solid State Device Research Conference* (Editions Frontieres, Gif-sur-Yvette, France, 1996), pp. 813–820.
[19]C. Jungemann, S. Keith, F. M. Bufler, and B. Meinerzhagen, "Effects of band structure and phonon models on hot electron transport in silicon," Electr. Eng. **79**, 99–101 (1996).
[20]C. Jungemann and B. Meinerzhagen, *Hierarchical Device Simulation. The Monte Carlo Perspective* (Springer, Wien, 2003).
[21]G. Gilat and L. J. Raubenheimer, "Accurate numerical method for calculating frequency-distribution functions in solids," Phys. Rev. **144**, 390–395 (1966).
[22]P. M. Marcus, J. F. Janak, and A. R. Williams, *Computational Methods in Band Theory* (Plenum, New York, 1971).
[23]M. V. Fischetti and S. E. Laux, "Monte Carlo analysis of electron transport in small semiconductor devices including band-structure and space-charge effects," Phys. Rev. B **38**, 9721–9745 (1988).
[24]M. Fischetti, "Monte Carlo simulation of transport in technologically significant semiconductors of the diamond and zinc-blende structures. I. Homogeneous transport," IEEE Trans. Electron Devices **38**, 634–649 (1991).
[25]C. Jacoboni and L. Reggiani, "The Monte Carlo method for the solution of charge transport in semiconductors with applications to covalent materials," Rev. Mod. Phys. **55**, 645–705 (1983).
[26]J. Mateos, T. González, D. Pardo, V. Hoel, H. Happy, and A. Cappy, "Improved Monte Carlo algorithm for the simulation of δ-doped AlInAs/GaInAs HEMTs," IEEE Trans. Electron Devices **47**, 250–253 (2000).
[27]C. A. Armiento and S. H. Groves, "Impact ionization in (100), (110), and (111) oriented InP avalanche photodiodes," Appl. Phys. Lett. **43**, 198–200 (1983).
[28]K. Brennan and K. Hess, "Theory of high-field transport of holes in GaAs and InP," Phys. Rev. B **29**, 5581–5590 (1984).
[29]L. W. Cook, G. E. Bulman, and G. E. Stillman, "Electron and hole impact ionization coefficients in InP determined by photomultiplication measurements," Appl. Phys. Lett. **40**, 589–591 (1982).
[30]G. M. Dunn, G. J. Rees, J. P. R. David, S. A. Plimmer, and D. C. Herbert, "Monte Carlo simulation of impact ionization and current multiplication in short GaAs diodes," Semicond. Sci. Technol. **12**, 111–120 (1997).
[31]H. Kim, H. Tian, K. Kim, and M. Littlejohn, "Electron velocity-field characteristics of $In_{0.52}Al0._{48}$ As," Appl. Phys. Lett. **61**, 1202–1204 (1992).
[32]A. Majerfeld, "Subthreshold velocity-field characteristics for bulk and epitaxial InP," J. Appl. Phys. **45**, 3681–3682 (1974).
[33]K. Taguchi, T. Torikai, Y. Sugimoto, K. Makita, and H. Ishihara, "Temperature dependence of impact ionization coefficients in InP," J. Appl. Phys. **59**, 476–481 (1986).
[34]I. Watanabe, T. Torikai, K. Makita, K. Fukushima, and T. Uji, "Impact ionization rates in (100) $Al_{0.48}$ $In_{0.52}$ As," IEEE Electron Device Lett. **11**, 437–438 (1990).
[35]T. H. Windhorn, L. W. Cook, and M. A. Haase, "Electron transport in InP at high electric fields," Appl. Phys. Lett. **42**, 725 (1983).
[36]A. You and D. Ong, "Monte Carlo modeling of high field carrier transport in bulk InP," in *ICSE 2000: Proceedings of the 2000 IEEE International Conference on Semiconductor Electronics* (IEEE, 2000), pp. 168–172.
[37]G. Zhou, A. Fischer-Colbrie, and J. Harris, Jr., "IV kink in InAlAs/InGaAs MODFETs due to weak impact ionization process in the InGaAs channel," in *Conference Proceedings: Sixth International Conference on Indium Phosphide and Related Materials* (IEEE, 1994), pp. 435–438.
[38]V. Palankovski and R. Quay, *Analysis and Simulation of Heterostructure Devices* (Springer-Verlag, Wien, 2004).
[39]S. Ramo, "Currents induced by electron motion," in *IRE Proceedings* (1939), Vol. 27, pp. 584–585.
[40]A. Tosi, A. Dalla Mora, F. Zappa, and S. Cova, "Single-photon avalanche diodes for the near-infrared range: detector and circuit issues," J. Mod. Opt. **56**, 299–308 (2009).
[41]J. Campbell and C. Hu, "Infrared single photon avalanche detectors," Phys. Status Solidi C **7**, 2536–2539 (2010).
[42]E. Charbon and S. Donati, "SPAD sensors come of age," Opt. Photonics News **21**, 35–41 (2010).